Modeling of daytime radiative cooling enhanced vapor-compression refrigeration systems — Supplementary Material

Davide Forte[a], Claudio Belotti[b], Lorenzo Pattelli[c], Matteo Morciano[a], Eliodoro Chiavazzo[a], Pietro Asinari[a,c], Matteo Fasano[a]

[a]*Department of Energy, Politecnico di Torino, Corso Duca degli Abruzzi 24, Torino, 10129, Italy*
[b]*Istituto Nazionale di Ottica (CNR-INO), Via Madonna del Piano 10, Sesto Fiorentino, Firenze, 50019, Italy*
[c]*Istituto Nazionale di Ricerca Metrologica, Strada delle Cacce 91, Torino, 10135, Italy*

S1. Building

The single family building analyzed is composed of two conditioned stories and a non-conditioned attic. Floor useful area (A_b) and building gross volume (V) are equal, respectively, to 174 m^2 and 607 m^3. The main parts of the building such as walls, floor, roof, slabs, windows and doors were simulated as thermal masses (*Foundation, Thermal* library), while the air inside the rooms was simulated as moist air (*Foundation, Moist air* library). The values of thermal insulation of the different surfaces were derived from Tabula database [1]. Two different scenarios were considered: a building constructed between 1991 and 2005 (referred as *Standard building*) and a building constructed after 2005 (referred as *Modern building*). The different thermal transmittances of the building parts, in both scenarios, are reported in Tab. S1. From these transmittance values, a proper stratigraphy was constructed, using conventional materials in the building sector [2]. The detailed stratigraphy is displayed in Tables S2 and S3 for *Standard building* and in Tables S4 and S5 for *Modern building*. The optical properties of opaque and transparent surfaces exposed to the external environment, such as absorptivity in the solar spectrum, thermal emissivity and g-factor, are reported in Table S6.

Building type	U modern	U standard
Roof	0.74	2.20
Ext. walls	0.34	0.59
Upper slab	0.30	0.69
Lower slab	0.33	0.77
Windows	2.20	2.80
Doors	1.70	1.70

Table S1: Building thermal transmittance U (W m^2 K^{-1})

The building conditioned volume was modeled as a single item, neglecting the effect of internal building masses, such as internal walls, that were not simulated. The non-conditioned attic are separated from the conditioned space by an upper slab. The building facades are oriented towards the four cardinal directions, while the roof was assumed to be flat and perfectly horizontal.

For perimeter surfaces (walls, roof, floor, door, windows), the heat flow exchanged by conduction and convection was modeled as:

$$Q_{ext} = U_{ext} A_{ext} (T_{amb} - T_b) \tag{S1}$$

where A_{ext} is the opaque surface area, T_b is the air temperature of the room, T_{amb} is the external air temperature and U_{ext} is the surface global heat transfer coefficient, defined as:

$$U_{ext} = \frac{1}{\frac{1}{h_{int}} + \sum_n \frac{s_n}{L_n} + \frac{1}{h_{ext}}}. \tag{S2}$$

Internal air resistance ($1/h_{int}$) was assumed equal to 0.13 m^2 W K^{-1} for vertical surfaces and 0.17 m^2 W K^{-1} for horizontal surfaces except the roof, for which a value of 0.10 m^2 W K^{-1} was assumed [3]. For the external air resistance ($1/h_{ext}$) a value of 0.04 m^2 W K^{-1} was assumed for all the surfaces except the roof, for which h_{ext} was estimated as a function of wind velocity (v_w) using the correlation from Ref. [4]. For the building floor, the external convection was not present since the floor is assumed in direct contact with the ground and T_{amb} was assumed equal to the seasonal average air temperature.

Analogously, for the internal surfaces (lower slab), the heat flow exchanged by conduction and convection was modeled as:

$$Q_{int} = U_{int} A_{int} (T_{att} - T_b), \tag{S3}$$

where A_{int} is the opaque surface area, T_{att} is the attic temperature and U_{int} is the surface global heat transfer coefficient, defined as:

$$U_{int} = \frac{1}{\sum_{n=1}^{2} \frac{1}{h_{int,n}} + \sum_n \frac{s_n}{L_n}}. \tag{S4}$$

The windows thermal model accounted for the presence of the glass and the frame (the thermal resistances were considered in parallel between them). Therefore, the window heat transfer coefficient can be calculated as:

$$U_w = f_{gl} U_{gl} + (1 - f_{gl}) U_{fr} \tag{S5}$$

where U_{lg} and U_{fr} are, respectively, the glass and frame global heat transfer coefficients calculated using equation S2, and f_{gl} is the glass surface portion with respect to the total window surface. A value of 80% for f_{gl} was considered.

The incoming solar radiation transmitted through the transparent surfaces (windows) was calculated as:

$$Q_w = f_{gl} \, SF \, A_w g \Psi \cos(\theta_{sol,w}) \tag{S6}$$

	Materials	A	s_1	s_2	s_3	s_4
Ext. Walls	Hollow bricks (1), Rock wool (2), Air gap (3), Solid bricks (4)	223.33	6.0	4.0	5.0	20.0
Roof	Hollow bricks (1), Rock wool (2), Tiles (3)	96.4	4.0	0.8	1.0	-
Lower slab	Tiles (1), Rock wool (2), Concrete (3)	96.4	0.1	1.8	5.0	-
Upper slab	Hollow bricks (1), Rock wool (2), Concrete (3)	96.4	4.0	1.5	5.0	-
East window	Glass (1,4) with multi-Argon gaps 80% (3), Pine wood frame 20% (2)	6.52	0.4	1.2		0.4
South window	Glass (1,4) with multi-Argon gaps 80% (3), Pine wood frame 20% (2)	8.69	0.4	1.2		0.4
West window	Glass (1,4) with multi-Argon gaps 80% (3), Pine wood frame 20% (2)	6.52	0.4	1.2		0.4
North window	Glass (1,4) with multi-Argon gaps 80% (3), Pine wood frame 20% (2)	0	0.4	1.2		0.4
Door	Pine wood (1)	2.4	4.7	-	-	-

Table S2: *Standard building* stratigraphy - geometry: A (m^2) surface area, s (cm) layer thickness.

	$\mathbf{R_1}$	$\boldsymbol{\rho_1}$	$\mathbf{c_{p,1}}$	$\mathbf{R_2}$	$\boldsymbol{\rho_2}$	$\mathbf{c_{p,2}}$	$\mathbf{R_3}$	$\boldsymbol{\rho_3}$	$\mathbf{c_{p,3}}$	$\mathbf{R_4}$	$\boldsymbol{\rho_4}$	$\mathbf{c_{p,4}}$
Ext. Walls	0.140	1200	840	1.026	100	850	0.140	1.225	1006	0.222	2000	840
Roof	0.093	1200	840	0.197	100	850	0.023	1700	840	-	-	-
Lower slab	0.001	1700	840	0.462	100	850	0.625	2000	880	-	-	-
Upper slab	0.093	1200	840	0.385	100	850	0.625	2000	880	-	-	-
East window	0.003	2500	840	0.102	425	2390	0.235	1.784	523	0.004	2500	840
South window	0.003	2500	840	0.102	425	2390	0.235	1.784	523	0.004	2500	840
West window	0.003	2500	840	0.102	425	2390	0.235	1.784	523	0.004	2500	840
North window	0.003	2500	840	0.102	425	2390	0.235	1.784	523	0.004	2500	840
Door	0.416	425	2390	-	-	-	-	-	-	-	-	-

Table S3: *Standard building* stratigraphy - thermal properties: R (m^2 K W^{-1}) thermal resistance, ρ (kg m^{-3}) density, c_p (J kg^{-1} K^{-1}) specific heat capacity.

where A_w is the window area, g is the glass g-factor (in Tab. S6), Ψ is the solar irradiance and SF is the shading factor (a constant value of 0.9 was assumed for all windows). θ_{sol} is the solar incidence angle, defined as [5]:

$$\begin{aligned}\cos(\theta_{sol,w}) = &\sin(\psi)\sin(\delta)\cos(\beta_w) - \cos(\psi)\sin(\delta)\sin(\beta_w)\cos(\zeta_w)\\ &+ \cos(\psi)\cos(\delta)\cos(\omega)\cos(\beta_w)\\ &+ \sin(\psi)\cos(\delta)\cos(\omega)\sin(\beta_w)\cos(\zeta_w)\\ &+ \cos(\delta)\sin(\omega)\sin(\beta_w)\sin(\zeta_w)\,.\end{aligned} \tag{S7}$$

The latitude angle ψ depends on the geographical position of the building, β_w is the window tilt towards the horizontal and ζ_w is the window azimuth (or orientation) angle. The definitions of solar angle δ and hour angle ω can be found in Ref. [5]. The solar angles were calculated using the Solar Position Algorithm (SPA) developed by the National Renewable Energy Laboratory (NREL) [6].

The incoming solar radiation absorbed by the opaque external surfaces was defined as:

$$Q_{abs} = A_{ext}\alpha_{ext}\Psi\cos(\theta_{sol,ext}) \tag{S8}$$

where α_{ext} is the absorptivity in the solar spectrum of the external surface and $\theta_{sol,ext}$ is the solar incidence angle on the surfaces calculated with equation S7 at the external surfaces tilt and orientation. The remaining part of the incoming solar radiation on the opaque surfaces is reflected towards the environment. For the sake of simplicity, the thermal re-radiation effect of the external surfaces was neglected, except for the roof, where the phenomenon can be significant due to the high temperatures this surface can potentially reach. The equations used to model the roof re-radiation phenomenon are the same used to model the daytime radiative cooling (DRC) panels, as detailed in the main text.

Heat gains and losses due to ventilation were also taken into account, as the air within the conditioned environment was continuously exchanged to maintain good indoor air quality. Ventilation was modeled as an additional thermal flux:

$$Q_{vent} = zVc_{p,air}(T_{amb} - T_b), \tag{S9}$$

where $c_{p,air}$ is the air specific heat and z is the air change rate, which specifies how many times per hour the air within a room is replaced with fresh air. The parameter z accounts for air changes due to both intentional ventilation and infiltration, with a value of $0.45h^{-1}$ adopted [7]. Ventilation effects were not considered for the attic space, as it lacks windows and is not subject to regular air exchange.

Lastly, the effect of building internal thermal loads (people and electronic devices) is simulated as a constant thermal flux:

$$Q_{i.l} = q_{i.l}A_b \tag{S10}$$

where $q_{i.l}$ is the heat generated per unit surface, for which a value of 0.4 W m^{-2} was considered [7].

The building was modeled as a network of thermal resistances. Each internal or external surface consisted of one to four layers of different materials, each characterized by a thermal heat capacity and thermal conduction properties. Convection heat transfer was applied to surfaces exposed to the indoor environment and external air. The radiative heat transfer mechanism due to solar absorption was applied to external walls, the door and the roof, while solar transmission was considered only for the windows. Thermal re-radiation was accounted for exclusively on the roof surface exposed to the sky. Ventilation and

	Materials	A	s_1	s_2	s_3	s_4
Ext. Walls	Hollow bricks (1), Rock wool (2), Air gap (3), Solid bricks (4)	223.3	8.0	8.5	7.0	20.0
Roof	Hollow bricks (1), Rock wool (2), Tiles (3)	96.4	8.0	3.9	1.5	-
Lower slab	Tiles (1), Rock wool (2), Concrete (3)	96.4	0.1	7.0	8.0	-
Upper slab	Hollow bricks (1), Rock wool (2), Concrete (3)	96.4	8.0	6.3	10.0	-
East window	Glass (1,4) with multi-Argon gaps 80% (3), Pine wood frame 20% (2)	6.5	0.4	1.5		0.7
South window	Glass (1,4) with multi-Argon gaps 80% (3), Pine wood frame 20% (2)	8.7	0.4	1.5		0.7
West window	Glass (1,4) with multi-Argon gaps 80% (3), Pine wood frame (20%) (2)	6.5	0.4	1.5		0.7
North window	Glass (1,4) with multi-Argon gaps 80% (3), Pine wood frame (20%) (2)	0.0	0.4	1.5		0.7
Door	Pine wood (1)	2.4	4.7	0.0	0.0	

Table S4: *Modern building* stratigraphy - geometry: A (m^2) surface area, s (cm) layer thickness.

	R_1	ρ_1	$c_{p,1}$	R_2	ρ_2	$c_{p,2}$	R_3	ρ_3	$c_{p,3}$	R_4	ρ_4	$c_{p,4}$
Ext. Walls	0.186	1200	840	2.179	100	850	0.180	1.2	2000	0.222	2000	840
Roof	0.186	1200	840	0.987	100	850	-	0.0	1700	0.035	1700	840
Lower slab	0.001	1700	840	1.795	100	850	-	0.0	2000	1.000	2000	880
Upper slab	0.186	1200	840	1.615	100	850	-	0.0	2000	1.250	2000	880
East window	0.004	2500	840	0.131	425	2390	0.400	1.8	2500	0.004	2500	840
South window	0.004	2500	840	0.131	425	2390	0.400	1.8	2500	0.004	2500	840
West window	0.004	2500	840	0.131	425	2390	0.400	1.8	2500	0.004	2500	840
North window	0.004	2500	840	0.131	425	2390	0.400	1.8	2500	0.004	2500	840
Door	0.416	425	2390	-	-	-	-	-	-	-	-	-

Table S5: *Modern building* stratigraphy - thermal properties: R (m^2 K W^{-1}) thermal resistance, ρ (kg m^{-3}) density, c_p (J kg^{-1} K^{-1}) specific heat capacity.

	Standard			Modern		
	α	ε	g	α	ε	g
Ext. Walls	0.30	0.9	-	0.25	0.94	-
Roof	0.70	0.8	-	0.55	0.85	-
Door	0.30	0.9	-	0.25	0.94	-
Windows	-	-	0.75	-	-	0.67

Table S6: Surfaces optical properties: α absorptivity in the solar spectrum, ϵ thermal emissivity and g g-factor.

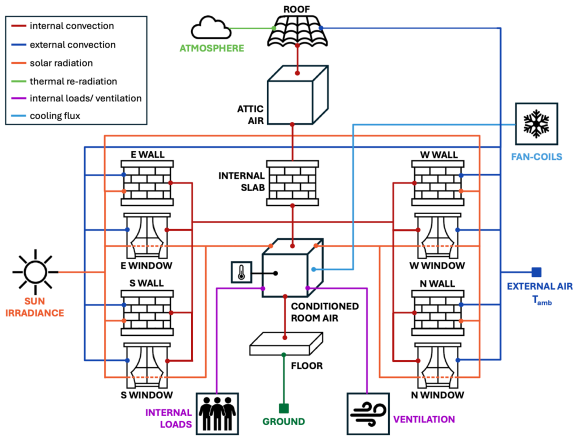

Figure S1: Schematic of the building model developed in *Simscape* environment.

internal loads were modeled as generic fluxes applied directly to the conditioned environment. A schematic representation of the building thermal network is shown in Fig. S1. All thermal masses, including air masses, were set to an initial temperature of 24 °C. In *Simscape* environment, the whole building system described before was modeled using *Thermal Mass*, *Conductive Heat Transfer* and *Convective Heat Transfer* blocks from *Foundation, Thermal, Elements*; *Controlled Temperature Source* and *Conductive Heat Flow Rate Source* from *Foundation, Thermal, Sources*; *Constant Volume Chamber* from *Foundation, Moist Air, Elements*.

S2. AC system

S2.1. Vapor-compression refrigeration system

The building cooling demand is met by an air-water vapor-compression refrigeration system (VCRS) using R1234yf as refrigerant fluid. The design constraints of the refrigerant cycle are reported in Tab. S7. The condenser temperature was set to 50°C to ensure that the VCRS operated effectively even on very hot days in locations like Las Vegas and Riyadh. To ensure a fair comparison between the different scenarios, this analysis assumed the same building structure and cooling system design across all tested locations. The design cooling demand was set equal to VCRS evaporator capacity and, knowing the enthalpy variation of the refrigerant inside the evaporator, it was possible to calculate the design refrigerant mass flow rate.

Tab. S8 presents the thermodynamic properties of R1234yf throughout the refrigerant cycle, while the ideal cycle is illustrated in Fig. S2. The transformation from state 1 to 2 represents the compression of the refrigerant, state 2 to 3 is condensation and subcooling within the condenser, state 3 to 4 is the isenthalpic expansion, and state 4 to 1 represents evaporation and superheating in the evaporator. The additional subcooling provided by the DRC panels increases the refrigerant cycle area by shifting state 3 further into the subcooled fluid region at lower

temperatures. The VCRS was modeled as a thermal system involving six components: evaporator, compressor, condenser, lamination valve, subcooler and a small tank for the refrigerant fluid.

The evaporator was designed as a counter-flow shell-and-tube heat exchanger, with R1234yf circulating on the tube side and a water-ethylene glycol (water-EG) mixture from the fan coil circuit on the shell side. The heat exchanger was properly sized to meet the cooling requirements, using *Logarithmic Mean Temperature (LMTD) method* for heat exchangers where one fluid undergoes a phase change [8] and the correlations for boiling fluids [9]. In *Simscape* environment, the evaporator was represented by the *Evaporator 2P-TL* block from the *Fluids, Heat Exchangers, Two Phase Fluid-Moist Air* library. The input parameters for this block are detailed in Tab. S9.

The air-cooled condenser was modeled as a cross-flow tube-fin heat exchanger with R1234yf on the tube side and moist air on the finned plate side. Air flows perpendicular to the bank of circular pipes, arranged in an inline configuration, and parallel to the plates. As with the evaporator, the condenser design is based on the *LMTD method* for heat exchangers involving phase change, with appropriate correlations for condensing fluids [9]. In the *Simscape* environment, the condenser was implemented using the *Condenser 2P-TL* block from the *Fluids, Heat Exchangers, Two Phase Fluid-Thermal Liquid* library. Input parameters for this block are provided in Tab. S10. The condenser fan was modeled using *Fan* block from *Fluids, Moist air, Turbomachinery* library (configured with an efficiency of 60% and a nominal speed of 1200 rpm), driven by an *Ideal Angular Velocity Source* block, from *Foundation, Mechanical, Mechanical Sources* library. The electric power consumed by the fan motor was determined as the product of Torque (T) and rotational speed (ω):

$$P_{\text{fan}} = T\omega. \tag{S11}$$

The torque was measured using the *Ideal Torque Sensor* block from *Foundation, Mechanical, Mechanical Sensor* library, while the rotational velocity was an imposed parameter. The mechanical efficiency of the fan motor was assumed to be 1. The power signal was then numerically integrated between the initial and final time, obtaining the electric energy consumed by the condenser fan $E_{\text{fan,c}}$.

The VCRS compressor was modeled using the *Positive-Displacement Compressor* block from the *Fluids, Two Phase Fluids, Fluid Machines* library driven by the already mentioned *Ideal Angular Velocity Source*. The compressor operated at nominal mass flow rate and at a nominal rotational velocity of 1000 rpm, with an isentropic efficiency of 75% and a volumetric efficiency of 95%. The inlet pipe is characterized by the same properties as the evaporator pipe, while the outlet pipe has the properties of the condenser tube. The electric power consumed by the compressor electric motor was calculated as the product of torque and rotational velocity:

$$P_{\text{cmp}} = T\omega, \tag{S12}$$

using the same procedure illustrated for the condenser fan electric motor. The power signal was then numerically integrated, obtaining the electric energy consumed by the compressor E_{cmp}.

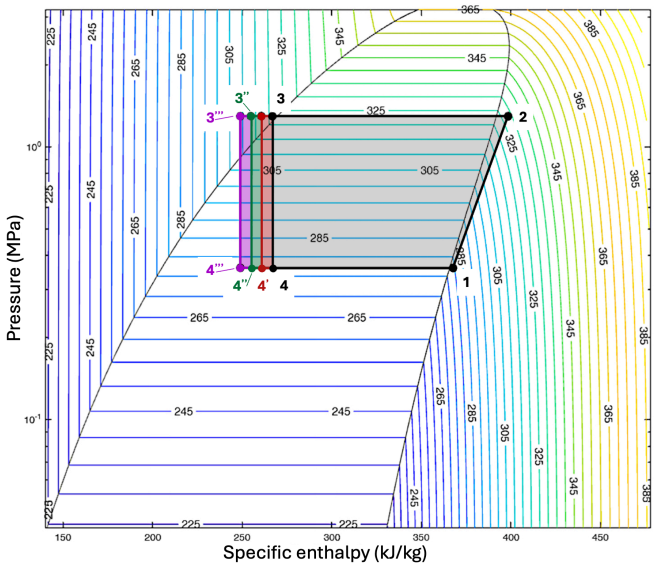

Figure S2: VCRS reference thermodynamic cycle. The points represent: 1-evaporator outlet, 2-condenser inlet, 3-condenser outlet in design conditions (design subcooling of 2°C), 4-evaporator inlet in design conditions. Points 3', 3" and 3"' represent the additional subcooling from DRC panels, respectively, -4 °C, -8 °C, -12 °C.

The thermostatic expansion valve was modeled using *Thermostatic Expansion Valve* block from the *Fluids, Two Phase Fluids, Valves & Orifices, Flow Control Valves* library. It operates by adjusting the orifice valve area in order to achieve the design evaporator super-heating. The VCRS is equipped with a small refrigerant fluid tank (block *Receiver Accumulator* from *Fluids, Two-Phase Fluids, Tanks & Accumulators*), positioned at the exit of the condenser, with a total volume of 1.9 L.

Parameter		
Evaporator temperature	4	°C
Condenser temperature	50	°C
Evaporator superheating	2	°C
Condenser subcooling	2	°C
Compressor isentropic efficiency	75%	
Refrigerant flow rate	0.0793	kg s^{-1}

Table S7: VCRS cycle design characteristics.

State	p (bar)	T (°C)	h (kJ kg^{-1})
1	3.61	6	367.78
2	13.02	55.1	398.38
3	13.02	48	266.68
4	3.61	6	266.68

Table S8: R1234yf thermodynamic properties.

S2.2. Fan-coil unit

The closed loop water-EG mixture circuit connects the VCRS evaporator to the indoor fan-coil unit (FCU). The cir-

Parameter		
Tube length	19.2	m
Number of tubes	2	
Tube inner diameter	0.21	m
Tube side internal surface roughness	0.0675	mm
Tube side fouling factor	0.01	K m^2 W^{-1}
Tube conductive resistance	0.0014	K kW^{-1}
Shell side free flow area	0.0021	m^2
Shell side heat transfer area	1.448	m^2
Shell side fouling factor	0.01	K m^2 W^{-1}

Table S9: Evaporator design parameters.

Parameter		
Tube length	44.8	m
Number of tubes	1	
Tube inner diameter	0.13	m
Tube internal surface roughness	0.0675	mm
Fouling factor	0.01	K m^2 W^{-1}
Tube conductive resistance	0.0013	K kW^{-1}
Tube rows along flow direction	4	
Tube segments in each tube row	8	
Longitudinal tube pitch	0.04	m
Transversal tube pitch	0.03	m
Total fin surface	41.6	m^2
Fin efficiency	61.0%	m
Air flow-rate	1.4	m^3 s^{-1}

Table S10: Condenser design parameters.

cuit contains also a circulation pump and a small tank. The indoor FCU was modeled as a cross-flow tube-fin heat exchanger with water-EG mixture flowing on the tube side and moist air on the finned plate side. Air flows perpendicular to the bank of circular pipes, arranged in an inline configuration, and parallel to the plates. The sizing procedure followed the same approach used for the air-cooled condenser in Section S2.1, with the only difference being that the correlations for the tube side are for a single-phase liquid [10]. In *Simscape* environment, the FCU was implemented using the *Heat Exchanger TL-MA* block from *Fluids, Heat Exchangers, Thermal Liquid-Moist Air* library. Input parameters for this block are provided in Tab. S11. The FCU fan was modeled analogously to the condenser fan. The fan electric power consumption was calculated using equation S11, and the signal was then integrated to obtain the electric consumption of FCU fan motor $E_{\mathrm{fan,b}}$.

The circulation pump was modeled as an ideal flow rate source (*Flow Rate source* block from the *Foundation, Thermal Liquid, Sources* library), delivering power isentropically. The power consumed by the circulation pump electric motor P_{pmp} was calculated as the product between the liquid volume flow rate ($\dot{V}$) and the pressure drops in the closed circuit (Δp):

$$P_{\mathrm{pmp}} = \dot{V}\Delta p. \tag{S13}$$

The volume flow rate and the pressure drops were measured, respectively, by a *Flow Rate Sensor* and *Pressure Sensor* from *Foundation, Thermal Liquid, Sensors* library. For the sake of simplicity, the mechanical efficiency of the electric motor was assumed to be 1. The signal of P_{pmp} over time was numerically integrated from the initial to the final time to calculate the energy consumption of the FCU circulation pump $E_{\mathrm{pmp,b}}$.

The liquid tank holds 10% of the total water-EG volume contained in the evaporator and FCU tubes and is set to a working pressure of 1.2 bar. It was modeled using the block *Tank* from the *Fluids, Thermal Liquid, Tanks & Accumulators* library.

Parameter		
Tube length	11.2	m
Number of tubes	4	
Tube inner diameter	0.10	m
Tube internal surface roughness	0.0675	mm
Fouling factor	0.05	K m^2 W^{-1}
Tube conductive resistance	0.0003	K kW^{-1}
Tube rows along flow direction	1	
Tube segments in each tube row	8	
Longitudinal tube pitch	0.04	m
Transversal tube pitch	0.03	m
Total fin surface	46.7	m^2
Fin efficiency	61.0%	m
Air flow-rate	1.17	m^3 s^{-1}

Table S11: FCU design parameters.

S2.3. Subcooler

A closed water-EG circuit couples the DRC panels to the VCRS condenser. This loop includes the subcooler, a circulation pump and a small tank. The sub-cooler was modeled as countercurrent tube-in-tube heat exchanger, with the water-EG mixture flowing on the shell side and R1234yf on the tube side. The heat exchanger size, defined by the design additional subcooling $\Delta T_{\mathrm{D,sc}}$, is a parameter analyzed during the parametric analysis. The *LMTD method* and the approach proposed by *Shah & Sekulic* [10] were used to calculate the tube-in-tube heat exchanger length for varying design subcooling. These calculations need as inputs the refrigerant and panel flow rates, as well as the condenser design outlet temperature, which are predetermined. The subcooler was sized to ensure that the pressure drop in the DRC closed loop remained below 10% of the nominal operating pressure (1.2 bar), to limit the impact on circulation pump consumption. The results of the sizing process are reported in Tab. S12.

The circulation pump of the radiative panels circuit was modeled equally to the FCU circuit circulation pump (section S2.2). The energy consumption of the DRC-circuit circulation pump $E_{\mathrm{pmp,p}}$ was calculated in the same manner as $E_{\mathrm{pmp,b}}$, by integrating Eq. S13 over the simulation period. The tank holds 10% of the total water-EG volume in the coupling circuit (including the panel serpentine and sub-cooler pipes) and helps smooth out pressure fluctuations. The tank was modeled using the block *Tank* from the *Fluids, Thermal Liquid, Tanks & Accumulators* library.

All dynamic simulations were carried out in the Simscape environment using the daessc solver, which is designed for differential-algebraic systems and supports variable-step integration. A relative tolerance and an absolute tolerance of 1e-3

Characteristic		
Pipe inner diameter	0.015	m
Shell inner diameter	0.040	m
Tube internal surface roughness	1.5	μm
Shell internal surface roughness	1.5	μm

Table S12: Subcooler design parameters.

were applied. Numerical convergence and physical consistency were verified for every simulation, and solver performance was evaluated using the Simulink Solver Profiler to confirm accuracy and stability. Each simulation ran smoothly and required between six to eight hours on a high-performance workstation with 128 GB of RAM and an Intel Core i7-13700HX CPU (2.1 GHz, 16 cores).

S3. DRC panels

The panel serpentine was sized in order to avoid pressure drops higher than 10% the nominal operating pressure. The geometry of a single DRC panel and the thermophysical properties of its constituent materials are reported, respectively, in Tables S13 and S14. The panel was modeled using a lumped-parameter approach, trying to simplify its geometry to achieve good computational performance. Consequently, the system was characterized by only two temperatures: the emitter temperature, which serves as the feedback signal for the lookup table, and the external pipe temperature. The thermal fluid flowing through the panels is a mixture of water and ethylene glycol (at 20%), pumped at an entering pressure of 1.2 bar. The panel thermal masses and the fluid inside the pipes were initialized at a temperature of 25 °C.

The thermal masses of the pipe and plate were modeled using the *Thermal Mass* block from the *Foundation, Thermal, Elements* library. The serpentine i was modeled by the *Pipe TL* block from the *Foundation, Thermal Liquid, Elements* library. Convection losses were modeled by connecting a *Convective Heat Transfer* block, which features a variable convective heat transfer coefficient (refer to the correlation with wind velocity described in the main text), between the emitter and the ambient environment, represented as a *Controlled Temperature Source*. Other flux components on the emitter were computed as detailed in the Methods section of the main text and applied to the emitter through a *Controlled Heat Flow Rate* source. The conductive heat transfer between the plate and the serpentine was modeled using a *Conductive Heat Transfer* block. The model for each DRC panel was constructed as a one-dimensional lumped model, operating under the assumption that the entire emitter is maintained at a uniform constant temperature. Multiple DRC panels were connected in series to form the DRC field. Field-level variables were obtained by averaging over all panels, meaning that the temperature, net flux, and radiative flux of the DRC field correspond to the average of the values recorded for each individual panel.

Characteristic		
Panel surface	1	m^2
Emitter thickness	0.3	cm
Serpentine diameter	3.8	cm
Serpentine thickness	0.1	cm
Serpentine specific length	4.0	m/m^2
Internal serpentine roughness	2	μm

Table S13: RC panel design parameters.

	Emitter	Serpentine	
Material	aluminum	copper	
Density	2700	8960	kg m^{-3}
Th. conductivity	240	400	W m^{-1} K^{-1}
Specific heat	900	385	J kg^{-1} K^{-1}

Table S14: RC panel thermophysical properties.

S4. Construction of DRC panels characteristic curve

The transient simulation results over the three-month period modeled were collected with a timestep of 10 seconds. The characterization of the DRC panels was conducted by considering the specific net cooling flux ($Q_{\text{net}}/A_{\text{p}}$) and the emitter subcooling (expressed as $T_{\text{e}} - T_{\text{amb}}$). Only data points corresponding to the DRC panel in operation (the VCRS compressor is running) were included in the analysis. Data points associated with the initial transient phase of the panel, which features spikes in the net cooling power Q_{net} due to significant temperature differences in the subcooler during startup, were excluded from consideration, as they are significantly influenced by thermal inertia. To implement this exclusion criterion, only data points occurring at least 10 minutes after the DRC panels started their operation were retained, as the transient spike duration was observed to range between 1 and 10 minutes.

The dataset was, then, partitioned into 100 equal bins between the maximum and minimum values of Q_{net}. The bins B are mathematically defined as follows:

$$B_k = \left[Q_{\text{net,min}}/A_{\text{p}} + (k-1)\Delta Q,\ Q_{\text{net,min}}/A_{\text{p}} + k\Delta Q \right] \quad \text{for } k = [1, 100] \tag{S14}$$

where

$$\Delta Q = \frac{\left(Q_{\text{net,max}} - Q_{\text{net,min}}\right)/A_{\text{p}}}{100}. \tag{S15}$$

For each bin, the arithmetic mean of the net flux and subcooling was computed:

$$\bar{Q}_{\text{net},k}/A_{\text{p}} = \frac{\sum_{i \in B_k} \left(Q_{\text{net}}/A_{\text{p}}\right)_i}{N_k} \quad \Delta\bar{T}_{e,k} = \frac{\sum_{i \in B_k} \Delta T_{\text{e},i}}{N_k}. \tag{S16}$$

Bins containing no data points were subsequently discarded. Finally, a linear regression was performed on the mean values of the remaining bins using the least mean square error method. The results of this data post-processing procedure are presented in Fig. S3 for the spectral selective with additional far infrared emissivity (SSFIR), ideal spectral selective (SS), ideal broadband (BB), commercial 1 (C1) and commercial 2 (C2) materials.

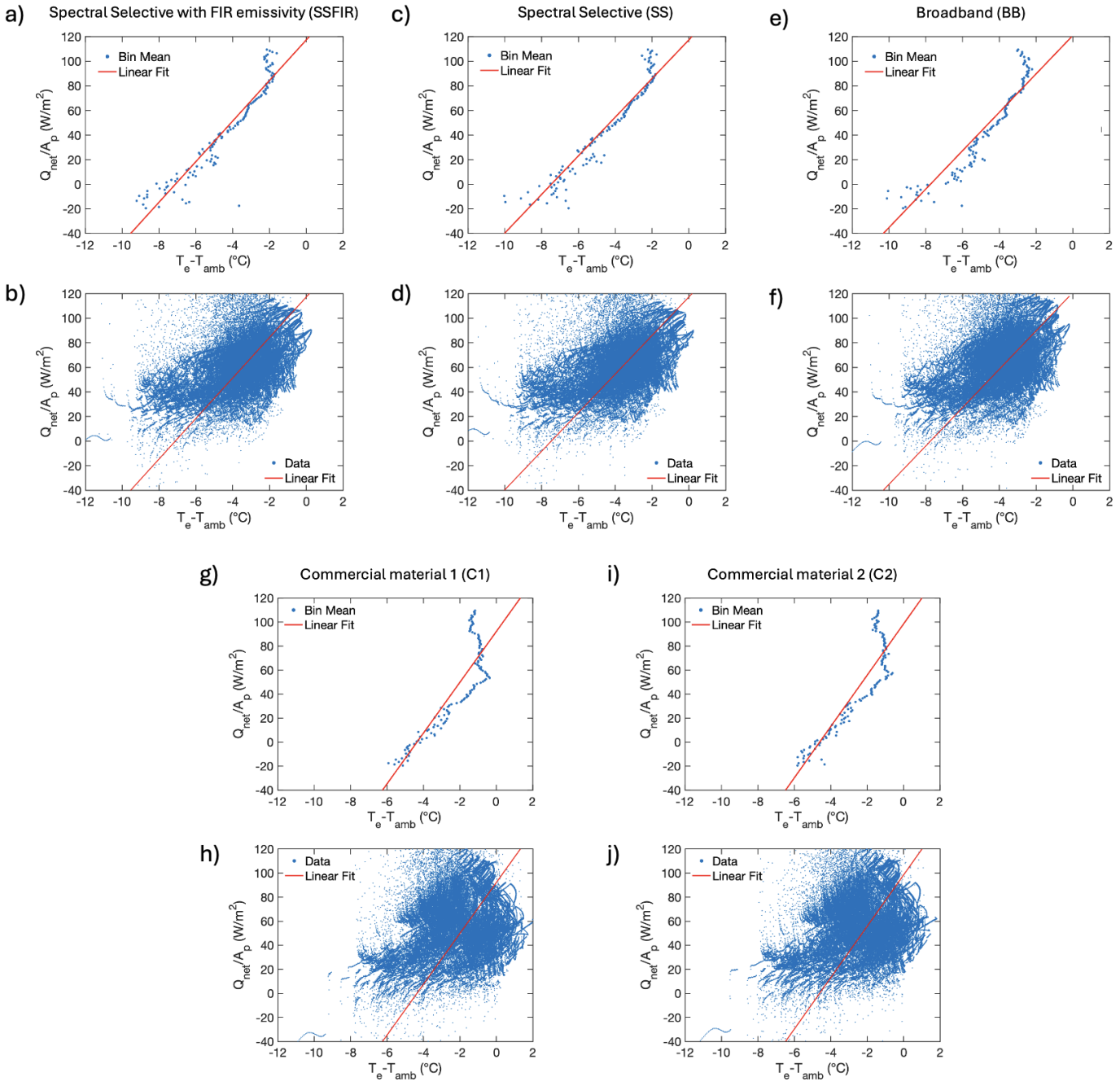

Figure S3: In the lower portion of each panel, scatter plots display the operational points of the DRC panels in $Q_{\text{net}}/A_{\text{net}}$ versus $T_{\text{e}} - T_{\text{amb}}$ plane for SSFIR, SS, BB, C1 and C2 emitters. These results are for a system with $A_{\text{p}} = 10\,\text{m}^2$, $G_{\text{p}}/A_{\text{p}} = 1.5\,\text{L}\,\text{min}^{-1}\,\text{m}^{-2}$, $\Delta T_{\text{D,sc}} = 12\,^{\circ}\text{C}$, located in Las Vegas and simulated with meteorological data of June-August; the cooling load is for the *Standard building*. In the upper part of each panel, linear regressions on the mean values of the bins for SSFIR, SS, BB C1 and C2 are shown, with R^2 values of 0.89, 0.84, 0.89, 0.75 and 0.79, respectively.

S5. Model validation

The hybrid cooling system proposed in this study consists of two main subsystems: a VCRS and an innovative DRC-driven subcooler. A component-wise validation strategy was employed, with the objective of validating each subsystem independently. The DRC-driven subcooler, which constitutes the primary novelty of this work, necessitates rigorous validation. For this reason, the outputs of the DRC material model were compared with experimental measurements obtained from a test facility of a partner institute in Madrid, as detailed in Ref. [11]. The experimental dataset corresponds to a 20 cm × 20 cm square specimen of DRC material mounted on a polystyrene support and positioned outdoors, horizontally, and directly exposed to the sky. The DRC specimen is a sample of SpaceCool Silver, corresponding to commercial material 1 (C1) described in the main text. Its emissivity spectrum is

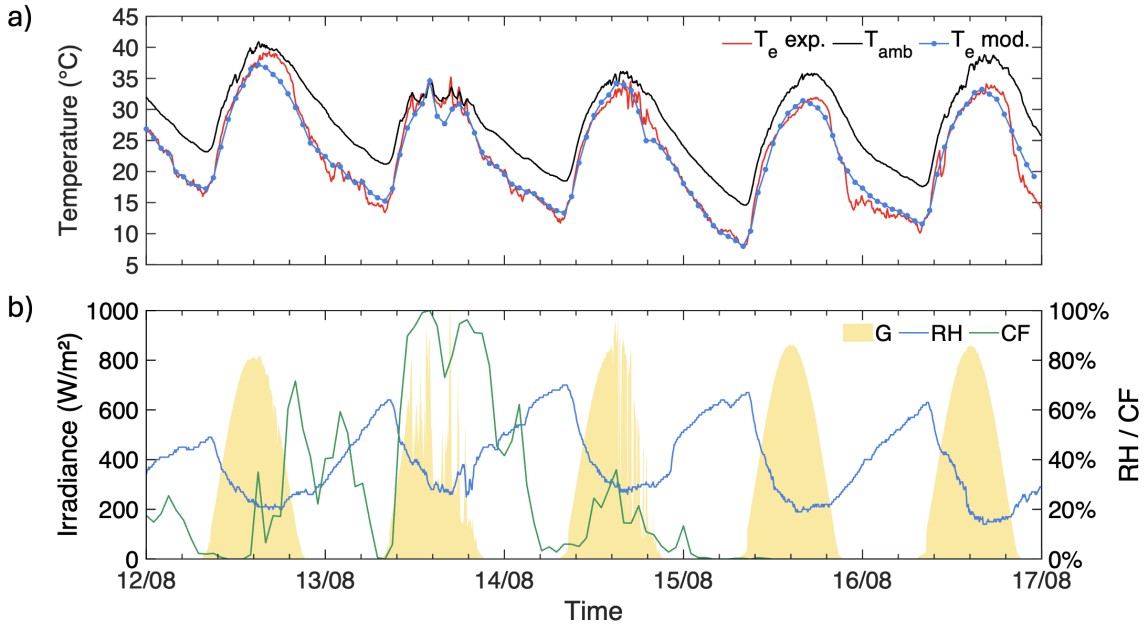

Figure S4: (a) Comparison between the temperature of the DRC sample predicted by the model (blue curve) and the experimental temperature (red curve). (b) Meteorological data used for the simulation: solar irradiance, relative humidity (RH) and cloud cover (CF).

presented in Fig. 2b. The material consistently exhibited surface temperatures below ambient, even during periods of high solar irradiance or under fully overcast conditions. The validation process exploited a continuous experimental record spanning over five consecutive days, from 12 to 16 August 2024. Input variables, including solar irradiance, ambient temperature, relative humidity, and wind speed, were acquired from an on-site meteorological station with a temporal resolution of five minutes. Atmospheric composition and cloud cover data, required for calculating downwelling atmospheric radiation, were obtained from the ERA5 reanalysis dataset with an hourly resolution. Validation results are presented in Fig. S4. The model reproduced the measured surface temperature with a mean absolute percentage error (MAPE) of 4.9 % and a root mean square error (RMSE) of 1.5 °C. Furthermore, the model accurately represented the thermal response of the DRC surface under moderately cloudy and fully overcast conditions, such as those recorded during midday on 13 August 2024. These findings confirm the validity of the DRC material model, as well as the suitability of the RRTM_LW for calculating the atmospheric radiative flux absorbed by the panel. The remaining components of the VCRS—namely, the condenser, evaporator, expansion valve, compressor, and fan coils—were implemented using pre-configured blocks available in the *Simscape* environment. Consequently, detailed validation of their internal thermodynamic behavior was considered unnecessary. Moreover, similar *Simscape*-based VCRS models have been validated in previous studies reported in the literature [12–14]. The verification process was therefore focused on confirming the correct sizing of each component. To this end, each subsystem was tested individually under steady-state boundary conditions representative of the design operating point. Following the initial transient, the steady-state outputs of all components matched their respective target values, thereby confirming the correctness both of the sizing and the implementation of the model.

Additional plots

A parametric analysis was conducted to evaluate the variation in energy savings achieved by the DRC system as a function of cooling demand. The VCRS size and building characteristics were held constant, while the internal generation parameter $q_{i,l}$ was varied to generate a curve relating energy savings to the the DRC-enhanced VCRS uptime. Fig. S5 illustrates this relationship for the *Modern building* in Turin climate with a DRC system featuring 8 m^2 of radiative area. The results indicate a linear increase in energy savings with VCRS uptime, highlighting the greater effectiveness of the DRC system in cooling-dominated climates with significant space cooling demand during the hot season.

Fig. S6 presents the results of a sensitivity analysis investigating the natural aging of DRC materials due to exposure to atmospheric agents, with particular emphasis on the effects of ultraviolet (UV) radiation. UV-induced degradation represents a critical durability concern for DRC materials. From an optical standpoint, UV radiation is known to deteriorate polymeric constituents, potentially reducing the solar reflectivity of DRC surfaces [15] Previous studies indicate that, while longwave emissivity is only marginally affected, shortwave reflectivity can experience substantial degradation, leading to a relevant reduction in cooling performance [16]. Based on the findings of this study and the material database of the Cool Roof Rating Council [17], the incorporation of aging effects into simulation models can be reasonably approximated by adjusting only the solar reflectivity

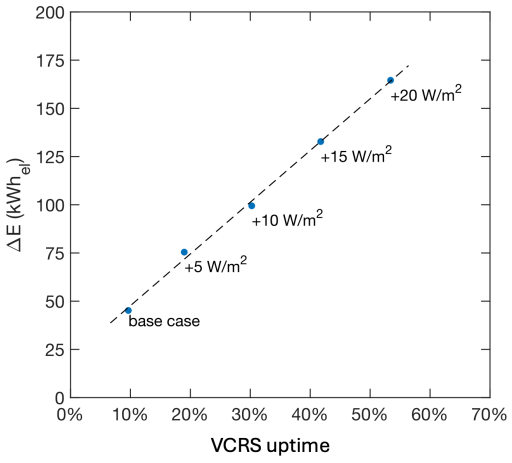

Figure S5: Electric energy savings as a function of VCRS uptime. The cooling demand of the building was modulated by varying the internal heat generation, as depicted in the plot, expressed in W m^{-2} of the conditioned building surface area. These results are for a system with $A_p = 8\,m^2$, $G_p/A_p = 1.5\,L\,min^{-1}\,m^{-2}$, $\Delta T_{D,sc} = 8\,°C$, located in Turin and simulated with meteorological data of June-August; the cooling load is for the *Modern building* and the panels are coated with the SSFIR material.

parameter of DRC materials. A reduction in solar reflectivity within the range of 1 % to 10 % was considered a representative estimate of natural aging effects. Fig. S6 illustrates the influence of solar reflectivity degradation on overall system performance, as well as on the net and radiative fluxes of the DRC panels. The reduction in electrical energy savings is expressed relative to the baseline case corresponding to an unaged material. A monotonic decline in relative energy savings is observed with decreasing solar reflectivity. Specifically, reductions in reflectivity of −3 %, −5 %, and −10 % correspond to decreases in energy savings of −6.3 %, −8.5 %, and −17.2 %, respectively. Both net and radiative fluxes display an approximately linear decrease as solar reflectivity diminishes.

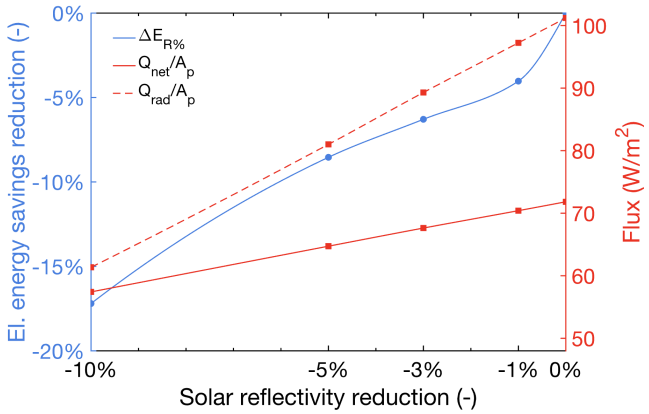

Figure S6: Impact of the decrease in solar reflectivity due to natural aging on electric energy savings, and net and radiative fluxes. These results are for a system with $A_p = 8\,m^2$, $G_p/A_p = 1.5\,L\,min^{-1}\,m^{-2}$, $\Delta T_{D,sc} = 12\,°C$, located in Las Vegas and simulated with meteorological data of June-August; the cooling load is for the *Standard building* and the panels are coated with the SSFIR material.

Fig. S7 illustrates the variation in the DRC circuit pump energy consumption relative to the total plant energy consumption ($E_{pmp,p}/E$) as a function of DRC surface area. The results indicate that the energy consumption of the DRC circuit pump remains below 1 % of the total plant energy consumption for DRC surface areas smaller than 10 m^2 across all evaluated locations.

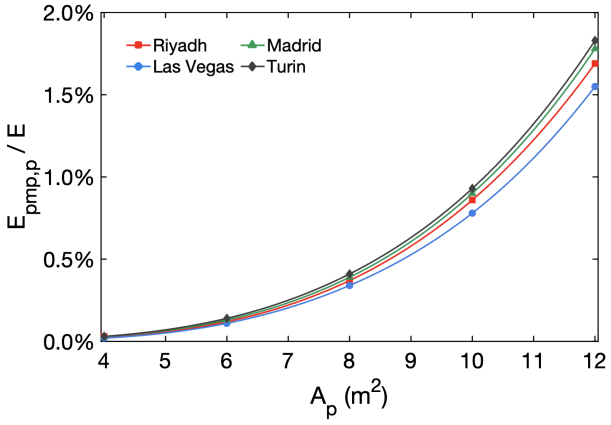

Figure S7: DRC circuit pump energy consumption (normalized over the total plant energy consumption) against DRC surface area. These results are for a system with $G_p/A_p = 1.5\,L\,min^{-1}\,m^{-2}$, $\Delta T_{D,sc} = 12\,°C$, simulated with meteorological data of June-August; the cooling load is for the *Standard building* and the panels are coated with the SSFIR material.

Figures S8, S9 and S10 presents results of the radiative transfer simulations carried out with RRTM_LW (panel a), together with the main atmospheric parameters (panel b) for Riyadh, Madrid and Turin, respectively. A comprehensive description of the physical quantities depicted is provided in the Main Text.

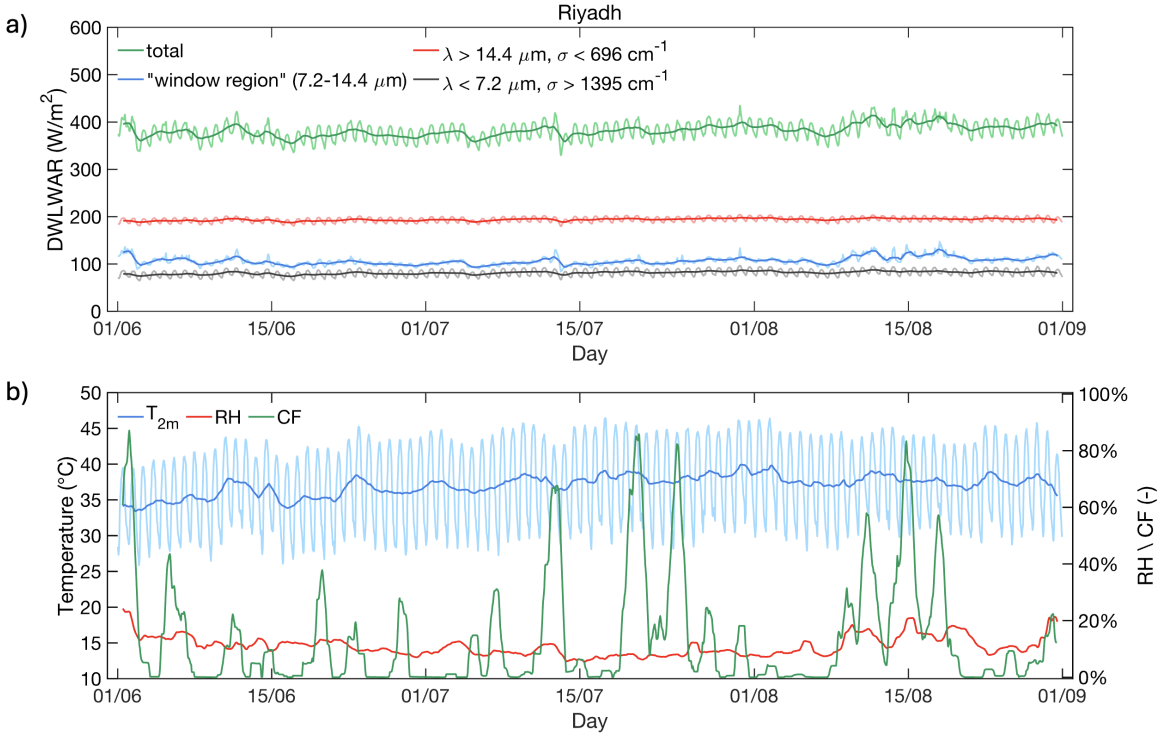

Figure S8: a) Time series of the downwelling atmospheric irradiance for Riyadh. (b) Time series for air temperature at 2 m (T_{2m}) above ground, relative humidity (RH) and cloud cover (CF).

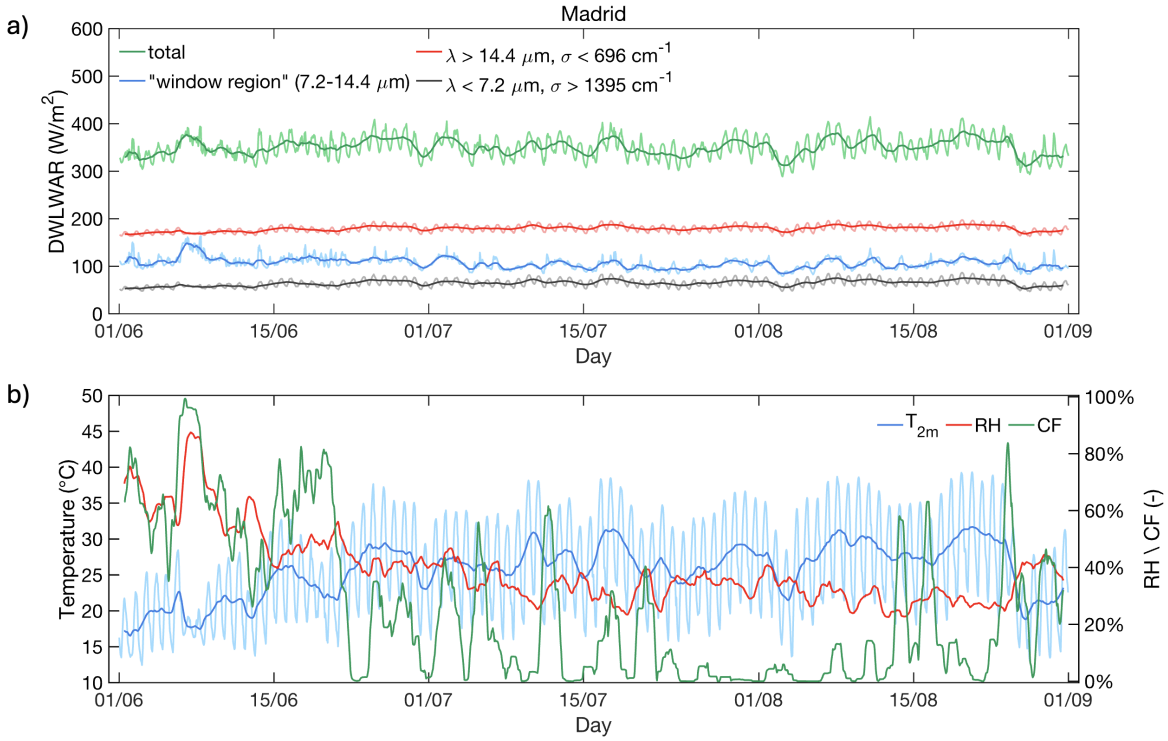

Figure S9: a) Time series of the downwelling atmospheric irradiance for Madrid. (b) Time series for air temperature at 2 m (T_{2m}) above ground, relative humidity (RH) and cloud cover (CF).

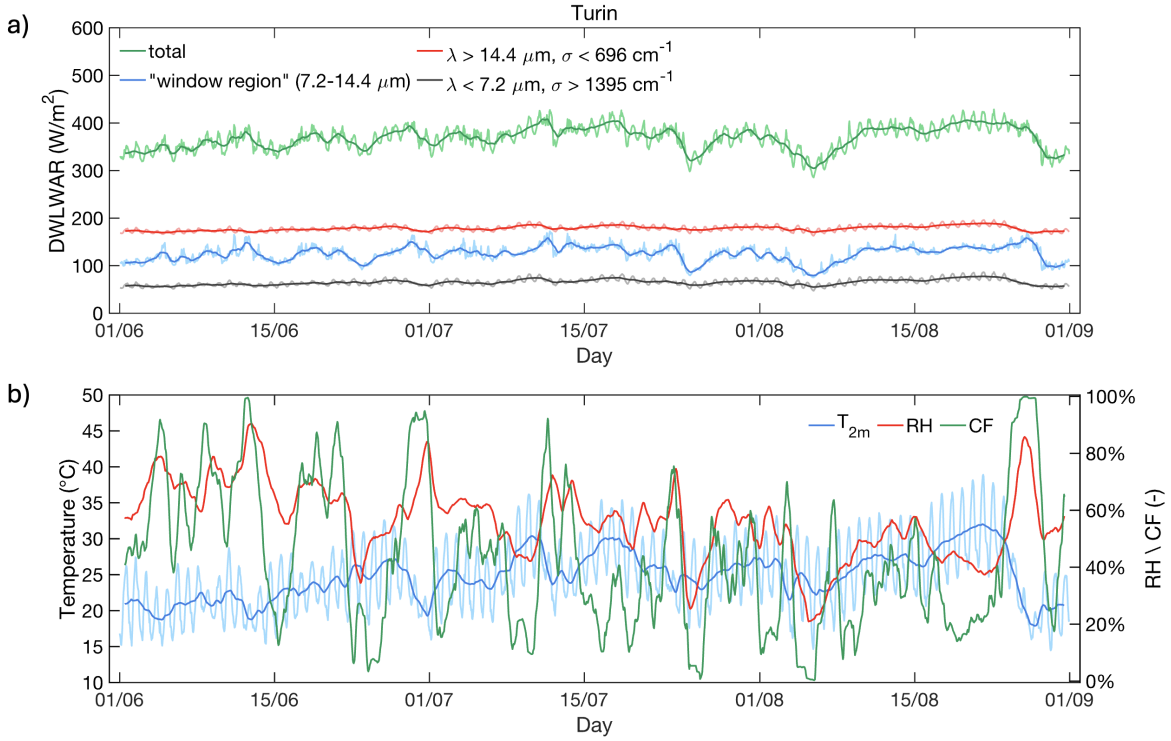

Figure S10: a) Time series of the downwelling atmospheric irradiance for Turin. (b) Time series for air temperature at 2 m (T_{2m}) above ground, relative humidity (RH) and cloud cover (CF).

References

[1] Tobias Loga, Britta Stein, and Nikolaus Diefenbach. Tabula building typologies in 20 european countries—making energy-related features of residential building stocks comparable. *Energy and Buildings*, 132:4–12, 2016.

[2] I Jankovic, X Fernandez, and J Diriken. Database of grey-box model parameter values for EU building typologies. *Ambience EU Project Report*, 2021.

[3] CIBSE. Chartered institution of building services engineers London. Environmental design CIBSE Guide A, 2006.

[4] S. Sharples and P. S. Charlesworth. Full-scale measurements of wind-induced convective heat transfer from a roof-mounted flat plate solar collector. *Solar Energy*, 62(2):69–77, 1998.

[5] Soteris A Kalogirou. *Solar energy engineering: processes and systems*. Elsevier, 2023.

[6] Meysam Mahooti. Nrel's solar position algorithm (spa). `https://www.mathworks.com/matlabcentral/fileexchange/59903-nrel-s-solar-position-algorithm-spaLastaccessed:14/06/2025`, 2025.

[7] Tobias Loga and Nikolaus Diefenbach. Typology approach for building stock energy assessment. TABULA calculation method-energy use for heating and domestic hot water-reference calculation and adaptation to the typical level of measured consumption-TABULA documentation-TABULA project team, 2013.

[8] Frank P. Incropera, David P. DeWitt, Theodore L. Bergman, Adrienne S. Lavine, et al. *Fundamentals of heat and mass transfer*, volume 6. Wiley New York, 1996.

[9] Sadik Kakaç, Hongtan Liu, and Anchasa Pramuanjaroenkij. *Heat exchangers: selection, rating, and thermal design*. CRC press, 2002.

[10] Ramesh K Shah and Dusan P Sekulic. *Fundamentals of heat exchanger design*. John Wiley & Sons, 2003.

[11] E. González-Cruz, G. Pérez, F. Borja, C. Alonso, F. Martin-Consuegra, E. Krüger, A. Gutierrez, and B. Arranz. Full-scale facility for the assessment of night and daytime passive radiative cooling. In *Proceedings of 2024 CATE Conference, 20-22 November 2024 Seville, Spain*, page 179, November 2024.

[12] Dynamic modeling and validation of a carbon dioxide heat pump system. *Evergreen*, 7(2):172–194, June 2020.

[13] Jonadri Bundo, Denis Panxhi, and Donald Selmanaj. A black box approach to air source heat pump power output modelling. In *2024 IEEE 7th International Conference and Workshop Óbuda on Electrical and Power Engineering (CANDO-EPE)*, pages 000243–000248. IEEE, 2024.

[14] Marco Simonazzi, Nicola Delmonte, Paolo Cova, and Roberto Menozzi. An integrated building energy model in matlab. *Energies*, 18(11):2948, 2025.

[15] Jianing Song, Qingchen Shen, Huijuan Shao, and Xu Deng. Anti-environmental aging passive daytime radiative cooling. *Advanced Science*, 11(10):2305664, 2024.

[16] Yue He, Biao Lu, Jinzhong Fang, Yue Lei, Shan Gao, and Chi Feng. Radiative cooling for long-term building energy efficiency: an experimental comparison of seven coatings. *National Science Open*, 3(3):20230065, 2024.

[17] Crrc rated roof products directory. `https://coolroofs.org/directory/roof?orderBy=aged_solar_reflectance&sort=desc`, 2025. Accessed on 2025-08-1.